Multi-Contact Localization Framework for Flexible Robots Using a Data-driven approach

Xuan Thao Ha, Aditya Sridhar, Mouloud Ourak, Gianni Borghesan,
Arianna Menciassi and Emmanuel Vander Poorten

***Abstract*—Minimally Invasive Surgery (MIS) is increasingly employed in several medical disciplines. During minimal invasive cardiovascular approaches, flexible instruments such as catheters or endoscopes are navigated along a tortuous path to reach a deeply seated target site. Navigation through the vasculature is not without risk as the vessel can be fragile, potentially with plaque or calcification that could get dislodged if excessive stresses are caused during navigation. Knowledge of the interaction forces between these flexible tools and the vasculature could help to steer the instruments and avoid exerting excessive forces on the surrounding tissues. Integrating force sensing into the tip of the instruments has been proposed in the art. However, tip force sensing is blind to forces that arise along the catheter body's length. This paper proposes a data-driven framework to estimate the locations of multiple contact forces along the catheter's length. The proposed approach consists of a contact state detection and subsequently a contact localization method. Both methods make use of knowledge of the shape of the catheter's body. This shape is measured here by a multi-core Fiber Bragg Grating (FBG) fiber. The proposed method also works for steerable catheters as it allows accounting for the effect of the actuation of the catheter itself. A state-of-the-art contact localization method using multi-core FBG fiber is implemented and serves as a baseline to compare the newly proposed method with. The proposed data-driven approach requires a minimum amount of training data which can be collected by simply actuating the robotic catheter in free-space over its workspace. The method is validated with a commercial MitraClip steerable guide catheter. Dynamic experiments show that the proposed contact state detection method can detect contact in** 0.44 **seconds. The average contact localization errors of the proposed method and state-of-the-art method are** 6.1 **mm (**1.6%**) and** 18.0 **mm (**4.9%**), respectively.**

I. INTRODUCTION

Flexible robots (FRs) are increasingly being used in clinical applications thanks to their ability to reach the surgical site via tortuous lumens. Despite the significant compliance that allows the robot shape to conform to the surrounding anatomy, accurate navigation of the FR remains a challenging task for physicians. Exerting large force on soft tissue can cause a variety of complications such as dislodgment of calcium or plaque, bleeding or ischemic complications [1]. This problem can be avoided by providing clinicians with quantitative insights on the governing interaction forces that are exerted on the surroundings by the catheter.

Different sensors have been proposed to estimate the interaction force. Miniaturized force sensors have been designed and attached to the FR's tip [2]–[5]. These tip force sensors complicate the FR's design and cause additional issues due to the sterilizing process. To overcome these problems, methods that make use of the FR's kinematic model together with an optical or a shape sensor for tip force estimation have been proposed [6], [7]. However, these approaches are not generalizable since developing a specific kinematic model is time-consuming and not very accurate. To avoid the complex kinematic modeling process, a learning-based approach to estimate tip force of a tendon-driven continuum manipulator using tendons' tension and position as inputs has been proposed by Feng *et al.* [8]. At the same time, optical fiber with Fiber Bragg Grating (FBG) sensors are becoming popular lately in the medical robotic field thanks to their small size, lightweight and high compliance. This allows them to be incorporated into the FRs with a limited effect on the mechanical property of the robots. E.g. a tip force sensor has been produced by combining a force-sensitive flexure with FBG sensors [9]–[11]. However, including additional force sensors to measure forces that act along the catheter body is not practical. Methods based on the kinematic model and the FR's shape to estimate the contact state and contact location along the length of FRs have been proposed in [12], [13]. As previously mentioned, the non-ideal behavior of the actuator and the transmission system may result in complex phenomena like friction, hysteresis, or backlash. These make it difficult to develop an accurate kinematic model of the robotic catheter. Some researchers propose to estimate the contact force along the FR using only shape. The latter can be estimated by a vision system [14] or FBG sensors [15]–[17]. In these approaches, one typically estimates the curvature along the FR's length together with the mechanic model of the rod to estimate the contact force. Despite promising results, many prior works are limited to passive systems. E.g Qiao, Al-ahmad and Diezinger use a passive Nitinol rod [14]–[17].

Curvature-based contact force estimation typically employs a two-step approach. After localizing the contact location, in a second step, the force amplitude can then be estimated. The contact localization technique significantly impacts the accuracy of the estimated amplitude or direction. Once contact

This work was supported by the ATLAS project. This project has received funding from the European Union's Horizon 2020 research and innovation programme under the Marie Sklodowska-Curie grant agreement No. 813782. This work has received funding from the European Union's Horizon 2020 research and innovation programme under grant agreement No. 101017140, the ARTERY project. This work was also supported by CURE a KU Leuven internal project (3E210658).

X.T. Ha is with the Department of Mechanical Engineering, KU Leuven, Belgium, and also with The BioRobotics Institute, Scuola Superiore Sant'Anna, Italy (email: xuanthao.ha@kuleuven.be)

A. Sridhar, M. Ourak and E. Vander Poorten are with the Department of Mechanical Engineering, KU Leuven, Belgium (email: aditya.sridhar@kuleuven.be; mouloud.ourak@kuleuven.be; emmanuel.vanderpoorten@kuleuven.be)

G. Borghesan is with the Department of Mechanical Engineering, KU Leuven, Belgium, and also with Flanders Make, Belgium (email: gianni.borghesan@kuleuven.be)

A. Menciassi is with The BioRobotics Institute, Scuola Superiore Sant'Anna, Italy (email: arianna.menciassi@santannapisa.it)

Digital Object Identifier (DOI): see top of this page.

locations have been accurately identified, the direction and magnitude of the contact force can be estimated using e.g. a rigid link model [18] or a Cosserat rod model [7]. This fact sets the initial point of this work as this paper focuses on developing an approach to precisely estimate the contact locations. Along these lines, our prior work [19] showed that it is possible to train an AutoEncoder to detect collisions solely by comparing the measured data with data obtained from free-space motion. The same free-space data could in principle be used to train multiple data-driven free-space curvature models which can estimate the contact location over the length of the FR. However, the previously proposed approach was only verified with one contact force. In this paper, a new data-driven framework to estimate the contact state and localize multiple contact points is presented. As in previous work [19], the training effort is kept low only relying on gathering free space curvature information. A new contact state detection method is proposed in this paper without the necessity to train an AutoEncoder. In the previous work [19], the contact location is estimated by identifying the discontinuity in the tip estimation error. Unlike [19], the new contact localization method localizes the contact point by directly comparing the curvatures estimated by the free-space curvature models with the curvatures measured by a multi-core FBG fiber. The proposed approach is validated in 2D and 3D by simultaneously applying multiple external forces at a MitraClip steerable guide catheter (Abbott Laboratories, IL) with a multi-core FBG fiber inserted into the central working channel. One of the key benefits of the proposed contact localization framework over existing approaches in the art is that the method is capable of estimating the curvatures caused by external forces independent of the actuation force that is used to bend the steerable catheter in a certain direction. From the curvatures that are caused by the external forces only, the direction and magnitude of the contact forces could be subsequently estimated using the method proposed in [7]. The traditional Cosserat rod-based contact localization approach requires the entire shape of the FR to be measured. Unlike the Cosserat rod-based approach, the proposed data-driven method can estimate contact locations for any segment along the catheter's length which is shape-sensitive.

The rest of the paper is organized as follows: Section II presents the contact localization framework which consists of a collision detection and a contact localization method. The experimental setup to verify the proposed framework and the experimental results are detailed in Section III. Finally, Section IV concludes the work and sketches directions of future work.

II. Multi-contact localization framework

The here proposed data-driven contact localization framework is based on discrete curvatures measured along the FR's shape. A method to estimate the curvatures using FBG sensors is detailed in Section II-A. The recorded discrete curvatures during free-space movement are then used to create the free-space curvature models for the FR. By comparing the output of the free-space curvature models and the actual curvatures measured by the multi-core FBG fiber, it is possible to detect the contact state of the FR. Details of the contact detection method are presented in Section II-B. After contact is observed, as described in Section II-C, the method can be used to determine the expected location(s) of the contact(s). Note that throughout this work the following assumptions are made:

- the instrument under investigation has a relatively large compliance, although already much lower than the Nitinol rod's compliance used in [14]–[17];
- the system is subject to point forces, i.e. distributed forces are not considered;
- for simplicity a multi-core FBG fiber is located centrally in the catheter, although the method is expected to work if the fiber would have been positioned off-center as well;

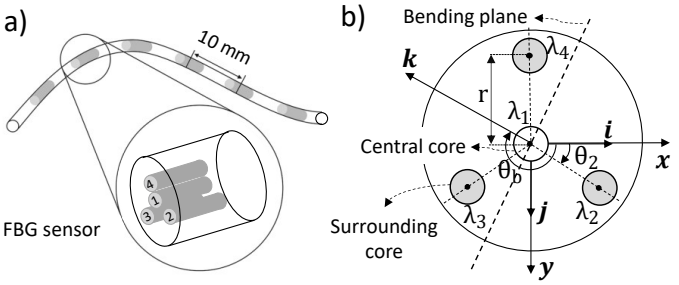

Figure 1. Figure a) shows a side view of a four-core FBG fiber while a cross-section view of the fiber is described in b). The angle of the bending plane and the angle of the 2^{nd} core with respect to the x-axis are denoted as θ_b and θ_2 in b), respectively. The radial distance between the central core and the surrounding core is denoted as r. The longitudinal distance between two consecutive sets of grating is 10 mm.

A. Multi-core FBG fiber-based curvature estimation

A multi-core FBG-based 3D shape estimation method relies on the strains that are measured by different FBG sensors distributed along the length of the multi-core fiber. Each FBG sensor is a Bragg reflector that reflects a limited band of the incoming light's spectrum while transmitting the remaining part of the spectrum to the following grating. The gratings in one core are designed in such a manner that the central wavelength of the reflected spectrum is separated from the others. Hence, it is possible to clearly distinguish the reflected light from one grating to that of the other gratings. The reflected wavelength of a grating is named Bragg wavelength λ_B. The Bragg wavelength λ_B varies depending on the environment's temperature variation ΔT and the mechanical strain ε applied to the grating. The reflected wavelength of each grating can be measured by an interrogator connected to the fiber. The relation between the wavelength shift of a fiber, the temperature variation ΔT, and the mechanical strain ε is given by:

$$\frac{\lambda_B - \lambda_{B_0}}{\lambda_{B_0}} = \frac{\Delta\lambda}{\lambda_{B_0}} = S_\varepsilon \varepsilon + S_T \Delta T, \tag{1}$$

where λ_{B_0} is the Bragg wavelength of the grating when in an unstrained state and λ_B is the current measured Bragg wavelength. The strain and temperature sensitivity coefficients are denoted as S_ε and S_T, respectively.

A multi-core FBG fiber used for 3D shape sensing normally has a central core ($i = 1$) that is aligned with the neutral axis of the fiber and three surrounding cores ($i = 2, 3$ and 4) as shown in Fig.1. The central core is only sensitive to axial strain and temperature variations. If the axial strain is negligible, as is frequently the case in flexible instruments used in MIS, the wavelength shift caused by the temperature variations can then be calculated from the central core. The bend-induced strain on the surrounding cores can be calculated as:

$$\varepsilon_{Bend_{i\in\{2,3,4\}}} = \frac{\Delta\lambda_i}{\lambda_{B_{0i}} S_\varepsilon} - \frac{\Delta\lambda_1}{\lambda_{B_{01}} S_\varepsilon}. \tag{2}$$

The three surrounding cores allow thus measuring the bend-induced strains in three directions at each cross section where a set of gratings is present. The relation between the three bend-induced strains, the magnitude of the curvature k and the angle of bending plane θ_b is given by:

$$\varepsilon_{Bend_{i\in\{2,3,4\}}} = -kr\sin(\theta_b - \frac{3\pi}{2} - \theta_i), \tag{3}$$

where r is the radial distance from the surrounding core to the neutral axis of the fiber; the angle θ_i and θ_b are the angles of the i^{th} core and the angle of the bending plane corresponding to the x-axis of the fiber as shown in Fig.1b, respectively. The closed-form solution [20] of (3) is given by:

$$\begin{aligned} \mathbf{k}_{app} &= \sum_{i=2}^{4} \frac{\varepsilon_{Bend_i}}{r}\cos\theta_i\hat{i} - \sum_{i=2}^{4} \frac{\varepsilon_{Bend_i}}{r}\sin\theta_i\hat{j}, \\ k &= \frac{2|\mathbf{k}_{app}|}{3}, \\ \theta_b &= \angle\mathbf{k}_{app}, \end{aligned} \tag{4}$$

where $\hat{i}$ and $\hat{j}$ are the unit vectors along the x- and y-axes of the fiber's cross section (shown in Fig.1b), respectively. The magnitude of the curvature in x- and y-directions can then be calculated as follows:

$$\begin{aligned} k_x &= k\cos\theta_b, \\ k_y &= k\sin\theta_b. \end{aligned} \tag{5}$$

The 3D shape of the fiber can be reconstructed by integrating the measured curvatures as shown in [21]. The fiber shape is represented by a space curve as a function of arc length s. To improve the estimated shape and maintain a quasi-continuous curvature profile over the fiber's length, the set of discrete curvatures is normally interpolated before the curvature integration process takes place. Assuming that the arc length of the fiber is discretized into n points, the sets of interpolated curvatures in x- and y-directions are denoted as $\mathbf{k}_{x_m} = \begin{bmatrix} k_{x_1} & \dots & k_{x_n} \end{bmatrix}^T$ and $\mathbf{k}_{y_m} = \begin{bmatrix} k_{y_1} & \dots & k_{y_n} \end{bmatrix}^T$, respectively.

B. Collision detection method

Traditional contact detection methods [12] normally rely on the FR's kinematic model. Nevertheless, because of the non-ideal behavior of the actuator and the transmission system, developing a precise kinematic model for FRs is challenging. To overcome this problem, data-driven contact detection approaches have been proposed. A neural network model has been proposed to detect the contact state in [22]. This approach requires that non-contact and contact data is gathered to train the neural network. Since there are many possible contact situations the amount of data that needs to be collected quickly becomes prohibitively large. Our previous work [19] presents an AutoEncoder network that can detect contact. The advantage of employing an AutoEncoder network over the neural network model from [22] is that only free-space data is required to train the model. In this work, a new method to estimate the contact state of the FR is proposed. By directly comparing the measured curvatures with the curvatures estimated by *multiple* free-space curvature models, the contact state can be determined reliably. This even allows for avoiding the neural network (AutoEncoder) training procedure.

Multiple machine learning (ML) models are first used to approximate the FR's free-space curvature models. The underlying idea of the so-called free-space curvature model is that the FR behaves highly repeatable while moving in free-space. Therefore, the FR will always take on a relatively similar shape. This repetitive shape then establishes a relation between a curvature measured at one arc length to the set of curvatures at the other arc lengths. The free-space curvature ML models learn this relationship so that by knowing a single pair of curvatures (in x- and y-directions) at one arc length, all the other curvatures can be deduced. The estimated curvatures in x- and y-directions at the j^{th} point using curvature information from the i^{th} point (k_{x_i} and k_{y_i}) are formulated as $\tilde{k}_{x_{ij}}$ and $\tilde{k}_{y_{ij}}$, respectively. For a FR's length that is discretized into n points, n free-space curvature models can be produced. The i^{th} free-space curvature model uses curvature information from i^{th} point (k_{x_i} and k_{y_i}) as input. The output of the free-space curvature models i^{th} is $\tilde{\mathbf{k}}_{x_i} = \begin{bmatrix} \tilde{k}_{x_{i1}} & \dots & \tilde{k}x_{in} \end{bmatrix}^T$ and $\tilde{\mathbf{k}}_{y_i} = \begin{bmatrix} \tilde{k}_{y_{i1}} & \dots & \tilde{k}_{y_{in}} \end{bmatrix}^T$. To generate data for free-space curvature models, the FR is actuated in free-space to cover its workspace. During free-space motion, the curvatures along the length of the FR are estimated (using the method in Section II-A) and recorded. In this work, each free-space curvature model is fitted by a k-Nearest Neighbors (kNN) model [23]. This kNN model is one of the simplest yet effective ML methods for approximating a data set without requiring extensive training time. The kNN model is considered sufficient in this work to show the proof of concept of the proposed framework. Advanced ML models can be investigated in the future to enhance accuracy and reduce processing time.

In the case of a contact, the relationships in curvatures between different arc lengths learned by the free-space models are no longer valid. As a result, the curvatures estimated by the free-space curvature models will differ from those measured by the multi-core FBG fiber. It is then possible to determine contact events by examining the difference between the estimated and the measured curvatures. To monitor the difference in estimated curvatures ($\tilde{\mathbf{k}}_{x_{i=1,\dots,n}}$ and $\tilde{\mathbf{k}}_{y_{i=1,\dots,n}}$) and measured curvatures ($\mathbf{k}_{x_m}$ and $\mathbf{k}_{y_m}$), an error matrix $\mathbf{E}_k$ ($n \times n$

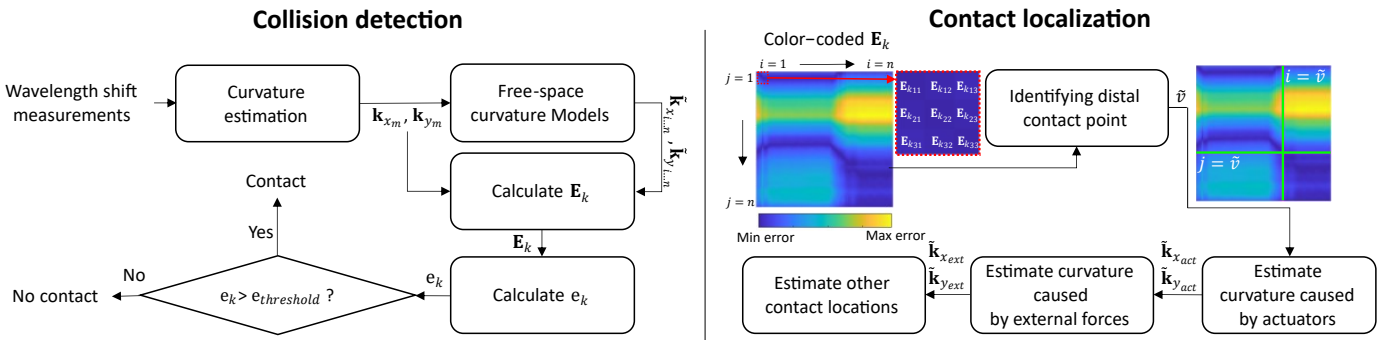

Figure 2. The proposed data-driven multi-contact localization framework consists of a contact detection phase and a contact localization phase. The contact detection first calculates the error matrix $\mathbf{E}_k$ based on the output of the free-space curvature models and the curvature estimated by the measured wavelength shift. A contact event can be detected by comparing the mean value of the error matrix $\mathbf{E}_k$ (denoted as e_k) with a threshold value $e_{threshold}$. In the case of a contact, the proposed contact localization method first determines the distal contact location based on the calculated $\mathbf{E}_k$. The color-coded graph of $\mathbf{E}_k$ can be seen in the panel. By knowing the distal contact location, the magnitude of the curvature in x- and y-direction ($\tilde{\mathbf{k}}_{x_{ext}}$ and $\tilde{\mathbf{k}}_{y_{ext}}$) solely can then be calculated. The other contact locations can be found at the points where the curvature profiles caused by the external forces display a discontinuity.

matrix) is formed as follows:

$$\begin{aligned} \mathbf{E}_{k_x} &= \begin{bmatrix} \mathbf{k}_{x_m} - \tilde{\mathbf{k}}_{x_i} & \dots & \mathbf{k}_{x_m} - \tilde{\mathbf{k}}_{x_n} \end{bmatrix} \\ \mathbf{E}_{k_y} &= \begin{bmatrix} \mathbf{k}_{y_m} - \tilde{\mathbf{k}}_{y_i} & \dots & \mathbf{k}_{y_m} - \tilde{\mathbf{k}}_{y_n} \end{bmatrix} \\ \mathbf{E}_k(i,j) &= \sqrt{\mathbf{E}_{k_x}(i,j)^2 + \mathbf{E}_{k_y}(i,j)^2} \end{aligned} \tag{6}$$

The element $\mathbf{E}_k(i,j)$ shows the difference in magnitude between the curvature estimated by the j^{th} free-space curvature model (using measured curvature at the j^{th} point) and the measured curvatures at the i^{th} point. The average curvature estimation error is then defined as

$$e_k = \frac{\sum_{i=1}^{n}\sum_{j=1}^{n}\mathbf{E}_k(i,j)}{n \times n}. \tag{7}$$

To detect if there is a contact, a threshold value $e_{threshold}$ can be imposed on e_k. The $e_{threshold}$ can be derived by calculating the mean error of e_k while the FR is moving in free-space. A contact event is detected when $e_k > e_{threshold}$. The calculated error matrix $\mathbf{E}_k$ is advantageously used in the next step to estimate the contact locations.

C. Contact localization method

Once the contact is detected, the contact localization method is used to identify the contact location. Previous works [15], [17] have shown that by identifying the discontinuities in the measured curvatures, the contact points can be detected in a straight rod. However, these approaches were not used for steerable continuum robots where the actuation itself induces strain variations on the robot's structure that are picked up by the FBG sensors. Assuming that the robot is actuated by tendons connected to the tip of the robot, the friction between the tendons and the lumens creates a non-uniform moment over the length of the continuum robot. As a result, there is a difference in the rate of change of curvature along the robot's length. In other words, the FR will not follow the commonly employed simplified constant curvature model e.g. employed in [24]. This reduces the accuracy of said contact localization methods when the robot experiences external forces and distributed moments induced by actuators simultaneously. The here proposed contact localization method addresses this problem, the method starts with identifying the last contact point that is closest to the distal end of the FR by analyzing $\mathbf{E}_k$ (presented in Section II-C1). To simplify the discussion this point is referred to as the "distal contact point" in the following. After identifying the distal contact point, the curvatures generated by the moment caused by the actuators ($\tilde{\mathbf{k}}_{x_{act}}$ and $\tilde{\mathbf{k}}_{y_{act}}$) can be calculated. Finally, the curvatures resulting from the remaining external forces ($\tilde{\mathbf{k}}_{x_{ext}}$ and $\tilde{\mathbf{k}}_{y_{ext}}$) can then be estimated by subtracting the curvatures caused by the actuators from the measured curvatures. The other contact points along the FR's length are finally determined by identifying the discontinuities in the magnitude of the curvature profiles that are associated with the external forces. These steps are detailed in Section II-C2. But first the method to derive the distal contact point is explained.

1) Identifying distal contact point: By analyzing $\mathbf{E}_k$, the distal contact point can be determined. Assuming that there are multiple point forces exerted on the FR and that the distal contact appears at the v^{th} point. Then, the free-space curvature relations between different arc lengths are only valid for the segment of the FR beyond the distal contact point i.e. from the $v+1^{th}$ to the n^{th} point. In other words, the elements $\mathbf{E}_k(p,q) \approx 0$ (where $p = v,\dots,n$ and $q = v,\dots,n$). Whereas the remaining elements will be greater than zero. In the ideal case, the distal contact point can be determined by finding the border of the region where $\mathbf{E}_k$ is 0. However, because the approximated free-space curvature models are not perfect, there are still small errors induced in $\mathbf{E}_k(p,q)$. To find the distal contact point, an optimization problem is formulated with the following cost function:

$$\arg\min_{\tilde{v}} \sum_{i=\tilde{v}}^{n} \left(D(\mathbf{E}_k(i,1:n),\tilde{v}) + D(\mathbf{E}_k(1:n,i),\tilde{v})\right), \tag{8}$$

where $\tilde{v}$ is the estimated distal contact point. The function $D(inputArr, brkPnt)$ splits the 1D input array $inputArr$ into two arrays at location $brkPnt$ and each split array is approximated by a straight line. The root-mean-square (rms) straight lines approximation error is returned by the function $D(.)$. Since $\mathbf{E}_k(p,q)$ is close to zero in an ideal case, the second

straight line is approximated by a line with a slope of zero. The function $D(.)$ is presented in Algorithm 1.

Algorithm 1 Calculate straight lines approximation error

Input: $inputArr_{n\times 1}, brkPnt$
Output: $error$

$n \leftarrow length(inputArr)$
$splitArr1_{brkPnt\times 1} \leftarrow inputArr(1 : brkPnt)$
$splitArr2_{(n-brkPnt)\times 1} \leftarrow inputArr(brkPnt+1 : n)$
$X_{brkPnt\times 2} \leftarrow \begin{bmatrix} 1_{brkPnt\times 1} & \begin{bmatrix}1 & \dots & brkPnt\end{bmatrix}^T \end{bmatrix}$
$inputArr_{fitted} \leftarrow \begin{bmatrix} X * (X \setminus splitArr_1) \\ mean(splitArr_2) * 1_{(n-brkPnt)\times 1} \end{bmatrix}$
$error \leftarrow rmse(inputArr, inputArr_{fitted})$

2) Multi-contact localization method: Once the distal contact point is determined, it is possible to estimate the curvatures caused by the actuators. Since the curvatures of the distal segment (after the distal contact point v^{th}) are caused by the distributed moment generated by the actuators only, the FR's curvatures caused by the actuators can be estimated by averaging the outputs of the free-space curvature models of the distal segment. The curvatures in the x-direction ($\tilde{\mathbf{k}}_{x_{act}}$) and y-direction ($\tilde{\mathbf{k}}_{y_{act}}$) resulting from the distributed moment can be estimated as follows:

$$\begin{aligned} \tilde{\mathbf{k}}_{x_{act}} &= \begin{bmatrix} \sum_{i=\tilde{v}+1}^{n} \frac{\tilde{k}_{x_{i1}}}{n-(\tilde{v}+1)} & \dots & \sum_{i=\tilde{v}+1}^{n} \frac{\tilde{k}_{x_{in}}}{n-(\tilde{v}+1)} \end{bmatrix}^T \\ \tilde{\mathbf{k}}_{y_{act}} &= \begin{bmatrix} \sum_{i=\tilde{v}+1}^{n} \frac{\tilde{k}_{y_{i1}}}{n-(\tilde{v}+1)} & \dots & \sum_{i=\tilde{v}+1}^{n} \frac{\tilde{k}_{y_{in}}}{n-(\tilde{v}+1)} \end{bmatrix}^T \end{aligned} \quad (9)$$

The curvatures in the x-direction resulting from the applying external forces can then be calculated by subtracting the curvatures caused by the actuator from the measured curvature ($\tilde{\mathbf{k}}_{x_{ext}} = \mathbf{k}_{x_m} - \tilde{\mathbf{k}}_{x_{act}}$). The curvatures in the y-direction ($\tilde{\mathbf{k}}_{y_{ext}}$) caused by external forces can be calculated in a similar way.

Let us consider the case in which the FR experiences a single point force at the v^{th} point. In such case, the curvatures caused by the external force should vary smoothly from the 1^{st} to the v^{th} point. However, if other external point forces are applied to the FR, the curvature profile will be disrupted. According to this observation, the remaining contact points in the proximal segment (before v^{th} point) can be found at the locations where $\tilde{\mathbf{k}}_{x_{ext}}$ and $\tilde{\mathbf{k}}_{y_{ext}}$ undergo a discontinuity. These locations can be found by e.g. applying the Piecewise Polynomial-Based Segmentation algorithm [17] on the external force curvature profiles. As the total number of external forces may be unknown, the Piecewise Polynomial-Based Segmentation algorithm iteratively varies the number of polynomial segments that are used to fit the input curvature. This iterative process is stopped when the fitting error is smaller than a pre-defined curvature threshold value. The intersections of the polynomial segments are considered as the other contact points. A more detailed implementation of the Piecewise Polynomial-Based Segmentation algorithm is illustrated in Algorithm 2. The MATLAB function $findBrkPnts(.)$ [25] computes the optimal location of the breakpoints based on a desired number of breakpoints. The input curvatures are approximated by a set of straight lines using the function $createSegments(.)$. Figure 2 summarizes the proposed data-driven multi-contact localization framework.

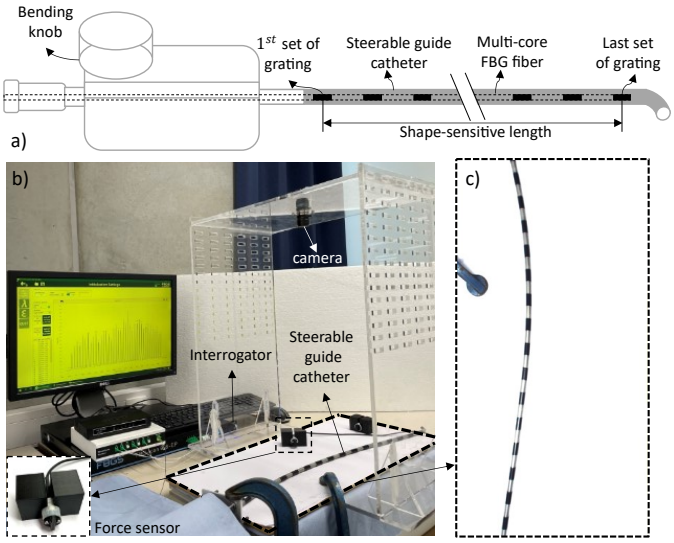

Figure 3. a) Schematic illustrating the employed method with a multi-core FBG fiber integrated in the steerable guide catheter of the MitraClip system. The shape-sensitive length starts from the position of the 1^{st} set of grating and ends at the last set of grating. In this work, a multi-core FBG fiber with 38 sets of grating is used, which leads to the shape-sensitive length of 370 mm. The experimental setup for 2D experiment is shown in b). Black markers are placed along the catheter's length which allows for projecting the 3D shape of the catheter to the image plane. The field of view of the overhead camera can be seen in c).

Algorithm 2 Piecewise Polynomial-Based Segmentation algorithm to find discontinuities in the curvature profiles

Input: $\mathbf{k}, e_{k_{threshold}}, N_{maxDisPnt}$
Output: $disPnts$

$i \leftarrow 1$
for $i < N_{maxDisPnt}$ **do**
  $disPnts \leftarrow findBrkPnts(i, \mathbf{k})$
  $\mathbf{k}_{fitted} \leftarrow createSegments(disPnts, \mathbf{k})$
  if $rmse(\mathbf{k}, \mathbf{k}_{fitted}) < e_{k_{threshold}}$ **then**
    return $disPnts$
  end if
  $i \leftarrow i+1$
end for

III. EXPERIMENTAL VALIDATION

A. Experimental setup

A steerable guide catheter of the MitraClip system is used to validate the proposed contact localization framework. This MitraClip device is used for transcatheter mitral valve repair. The steerable catheter is 630 mm long. It is actuated by two antagonistic steering wires running along the length of the catheter body that are connected to the tip of the catheter. These two steering wires allow the guide catheter to bend in a plane in two opposite directions. During the procedure, the steerable guide catheter is introduced from the femoral vein, traveling through a sequence of narrow vessels to reach the operational site (left atrium). While navigating through the fragile

vessels, it is important to avoid exerting too much force on the surrounding vessels which may cause various complications and consequently, reduce the procedure's success rate.

To localize the contact points along the guide catheter, a 0.38mm (outer diameter) four-core FBG fiber (FBGS, Geel, Belgium) is inserted into the central channel of the catheter. The employed fiber is made out of 38 sets of gratings (each set is spaced apart by 10 mm along the fiber's length). This leads to a total shape-sensing length of 370 mm. The schematic of the sensorized steerable guide catheter can be seen in Fig.3a. In this work, both 2D and 3D experiments are carried out. The 2D experimental setup includes four components: the sensorized steerable catheter, an interrogator - FBG-Scan 804 (FBGS, Geel, Belgium) connected to the multi-core FBG fiber to measure the wavelength shifts, an overhead monocular camera (Prosilica, Allied Vision Technology, Germany) and a 6 Degree-of-freedom force sensor (F/T Sensor nano17, ATI Industrial Automation, North Carolina, United States). The steerable guide catheter is placed on top of a plexiglass and is constrained by a mechanical clamp at the proximal end. During the 2D experiment, the force sensor is manually held. By doing so one can conveniently establish contact with the catheter at different locations along the shape-sensitive segment of the catheter. Contact can thus be applied and estimated between the first grating and the last grating (Fig.3a). In the first experiment, one external force is applied while in the second experiment, two external forces are applied. To hold the force sensor, a 3D-printed fixture is fabricated. The 3D-printed device is designed such that a point contact can be established between the force sensor and the steerable catheter. This makes the external point contact force assumption valid. A monocular camera is positioned approximately 500 mm above the catheter facing downward to capture the shape of the catheter as well as the position where the fixture establishes contact. This location serves as the ground truth that can be used to verify the performance of the proposed approach. The ground truth is generated by monitoring the magnitude of the force measured by the force sensor. The 3D shape of the steerable catheter is first reconstructed by the method proposed in [21] using the measured wavelength shifts. The 3D reconstructed shape is then mapped to the image frame thanks to visible markers attached along the catheter's length. Color segmentation is used to determine the markers and the contour of the obstacles in the image frame. The ground truth contact locations are the points in the image frame that corresponds to the mapped catheter shape and are closest to the obstacles' contours in the image frame. A nearest point search is then conducted with MATLAB's function *dsearchn* [26] The entire 2D experimental setup can be seen in Fig.3b. In the 3D experiment, the steerable catheter is clamped at the proximal end and actuated in free-space (not supported by the plexiglass). Two cables are wrapped around the catheter and pulled in two different directions as shown in Fig.5a-d. The cables are attached at the beginning of the optical markers. This enables contact location ground truth generation by knowing the correspondence between the optical markers and the arc length of the fiber.

A data set used to create free-space curvature models is recorded first. The steerable catheter is actuated in free-space to cover its workspace. During the free-space movement, the wavelength shifts are measured by the interrogator and are recorded to reconstruct the curvatures along the catheter's length. All sensors, including the camera, force sensor, and interrogator, are operating at 25 Hz during the data generation procedure for developing free-space curvature models and carrying out the tests. The robot Operating System (ROS) [27] is used to record and synchronize all the sensory data.

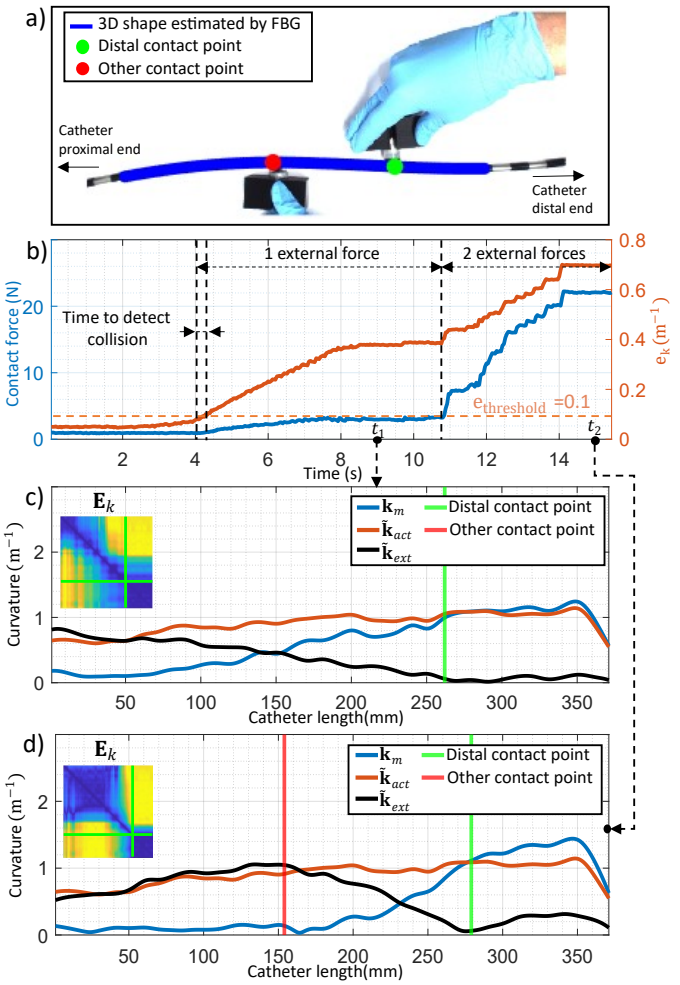

Figure 4. The result of an experiment when two external forces are applied to the catheter. The measured contact force (blue) and e_k (orange) are shown in b). The magnitude of measured curvature $\mathbf{k}_m$ (blue), of estimated curvature caused by actuators $\tilde{\mathbf{k}}_{act}$ (orange) and of estimated curvature caused by external force $\tilde{\mathbf{k}}_{ext}$ (red) at time $t = t_1$ and at time $t = t_2$ are shown in c) and d), respectively. Figure a) shows the image captured by the overhead camera at $t = t_2$. The two estimated contact points are shown in green (distal contact point) and in red (other contact point).

B. Results and discussion

The first 2D experiment (one force) is done by having the force sensor contact the catheter at 8 different locations while the catheter is bending to the left and to the right. In the second 2D experiment, 2 external forces are applied to the catheter at each time. The distal contact is first made by the force sensor. Another 3D-printed fixture is used to push the catheter in the opposite direction as can be seen in Fig.4a. Note that only one force sensor is used in the second experiment. The force

Table I
EXPERIMENTAL RESULTS OF THE 2D EXPERIMENT INCLUDING THE ESTIMATED CONTACT LOCATIONS AND THE CONTACT DETECTION TIME.

	Contact location (mm)						Detection time (s)	Contact location (mm)						Detection time (s)
	Ground truth		DiC		Proposed method			Ground truth		DiC		Proposed method		
	Distal	Other	Distal	Other	Distal	Other		Distal	Other	Distal	Other	Distal	Other	
One force	Left bending							Right bending						
	126	-	135	-	135	-	0.20	51	-	356	-	51	-	1.0
	164	-	151	-	151	-	0.20	89	-	135	-	94	-	0.68
	239	-	264	-	239	-	0.36	125	-	136	-	124	-	0.12
	279	-	262	-	288	-	0.40	164	-	188	-	170	-	0.20
Two forces	Left bending							Right bending						
	233	86	238	104	221	104	0.20	200	89	274	95	200	92	0.40
	273	120	316	120	274	120	0.32	237	90	289	106	234	98	0.56
	276	164	317	165	293	165	0.48	240	123	294	130	244	130	0.56
	311	202	318	198	318	198	0.88	278	161	336	157	277	155	0.44

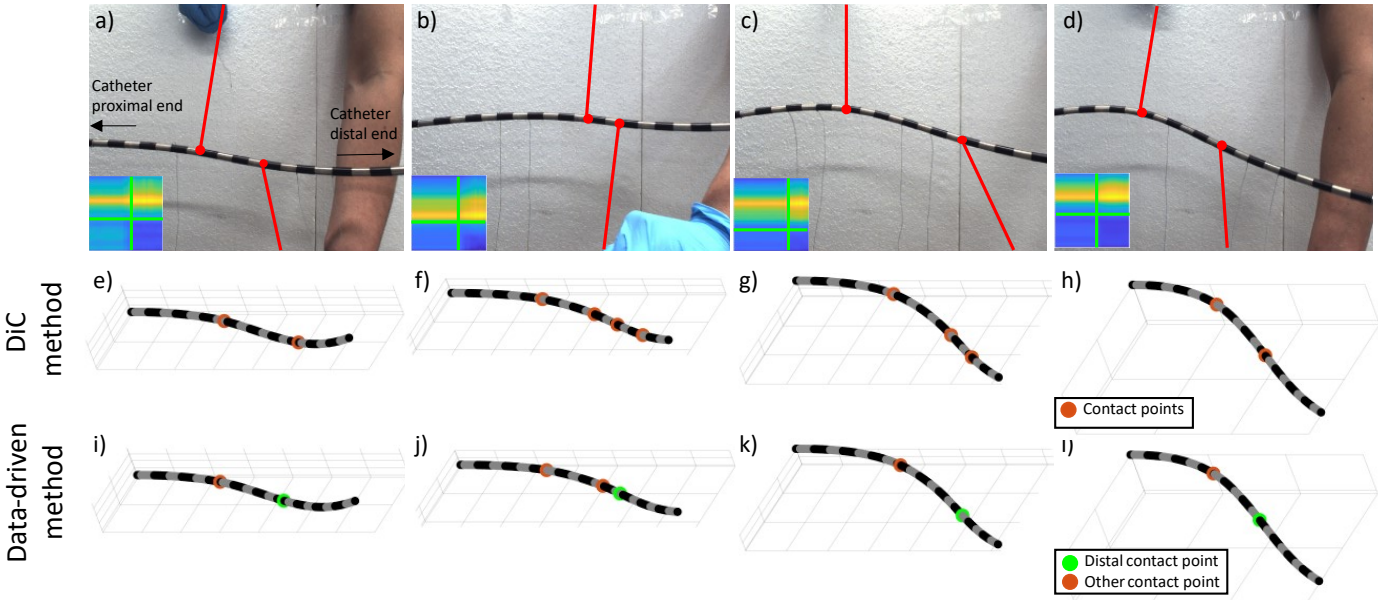

Figure 5. The 3D experiments are carried out with 2 external forces. The cables are wrapped around at the beginning of the optical markers and are pulled manually to apply point forces to the steerable catheter. Figures e-f show the estimated contact locations using the DiC method while figure i-l show the locations from the proposed data-driven method. The number of the estimated contact locations is larger than the actual number of contact forces in some cases (e.g. figure i,j,k). In such situation, the contact locations that are the closest to the ground truth are chosen and reported.

sensor is used to determine the contact detection time. This time is calculated as the time it takes from an increase in the contact force, i.e. the measured contact force, until the time contact is estimated as $e_k > e_{threshold}$. A second contact localization approach proposed in [17] is also implemented and compared to the proposed method. In this work, the second contact localization approach is called DiC since it is based on finding the discontinuity points in the measured curvature ($\mathbf{k}_{x_m}$ and $\mathbf{k}_{y_m}$) using the Piecewise Polynomial-based segmentation algorithm. These discontinuities are then considered as the contact locations.

An example result of the 2D experiment (two external forces) can be seen in Fig.4. In this experiment, the force sensor initially makes contact with the catheter at an arc length of 262 mm at $t = 4s$, while the catheter is actuated to bend to the right. The second contact occurs at $t = 10.7s$ at the arc length of 154 mm. The contact force measured by the force sensor (blue) and the mean value of $\mathbf{E}_k$ (orange) are shown in Fig.4b. It takes $0.28s$ to detect the contact event in the case when $e_{threshold}$ is set at 0.1 m^{-1}. The magnitude of the measured curvature ($\mathbf{k}_m = \sqrt{\mathbf{k}_{x_m}^2 + \mathbf{k}_{y_m}^2}$), of the estimated curvature caused by the actuators ($\tilde{\mathbf{k}}_{act} = \sqrt{\tilde{\mathbf{k}}_{x_{act}}^2 + \tilde{\mathbf{k}}_{y_{act}}^2}$) and of the estimated curvature caused by the external forces ($\tilde{\mathbf{k}}_{ext} = \sqrt{\tilde{\mathbf{k}}_{x_{ext}}^2 + \tilde{\mathbf{k}}_{y_{ext}}^2}$) at $t_1 = 9s$ and at $t_2 = 15s$ are plotted in Fig.4c and Fig.4d, respectively. The color-coded error matrix $\mathbf{E}_k$ at t_1 and t_2 are also shown in Fig.4. The estimated contact points using the newly proposed framework and the DiC approach together with the contact detection time of the 2D experiments are reported in Table I. It is worth mentioning that the number of contact locations estimated by the DiC is larger than the number of contact forces in some cases (see Fig.5f-g). In these cases, the contact locations that are closest to the ground truth are reported. The reported contact locations are collected when the catheter stops bending after colliding with obstacles. In other words, there is no longer an increase in the contact force. The experimental results show that the contact detection time varies due to the contact location. The contact event is detected faster in case the contact occurs in the middle of the catheter. The average contact detection time

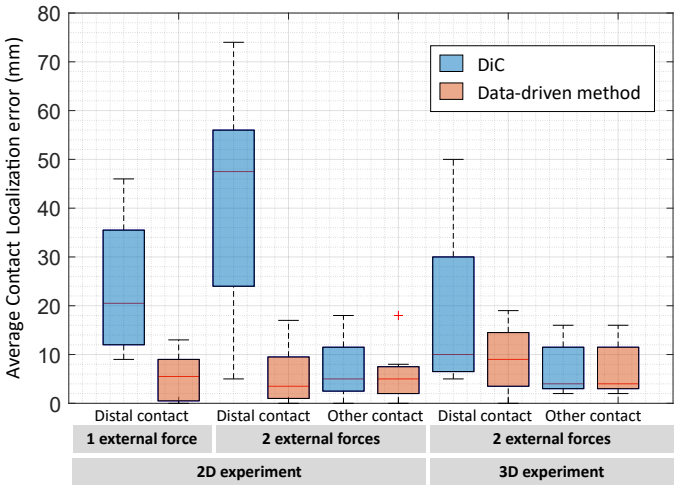

Figure 6. The quantitative average contact localization errors of the 2D and 3D experiments. Experimental results show the that proposed method has a consistent contact localization error of approximately 6.1 mm which corresponds to 1.6% of the shape-sensitive length of the fiber (370 mm).

in both experiments is 0.44*s*. Research has shown that the reaction time of the clinician is approximately 0.40*s* during MIS procedures [28]. Although the contact detection time of the proposed framework is a bit higher than the reported reaction time, it is worth noting that currently, clinicians have only limited haptic feedback while introducing the catheter into the patient's body. Thus, one can expect that tissue damage will be considerably reduced by having a method that can sense the contacts along the catheter's length. The average distal contact localization error of the DiC approach and the here proposed approach in the first 2D experiment (one force) are 20.7 mm and 5.4 mm, respectively. The average distal contact localization error of the proposed approach is approximately 75% higher than the DiC approach in the 2D one-force experiment. The contact towards the proximal end cannot be well estimated using the DiC approach as can be seen in the right bending case of the first experiment. A similar trend can be seen in the second 2D experiment (two forces) in which the average distal contact localization error of the DiC approach and the proposed approach are 41.8 mm and 5.6 mm, respectively. The accuracy of the newly proposed method is approximately 85% higher than the DiC approach. In contrast, both methods' average proximal contact localization errors in the 2D two-forces experiment show similar accuracy. The average estimated contact location errors are found to be 7 mm and 5.9 mm for the DiC and the here proposed approach, respectively. This demonstrates that the DiC technique is less effective in finding contact locations of low-magnitude forces. In the two-forces 2D experiment, the proximal contact forces are comparatively larger than the distal contact force, allowing the DiC method to detect these contact points accurately. The results of the 3D experiment are shown in Fig.5. Figure 5e-h show the contact locations estimated by the DiC approach. The contact locations estimated by the newly proposed data-driven approach are plotted in green (distal contact) and red (other contacts) in Fig.5i-j. The average error in distal contact location estimation of the DiC approach and the data-driven approach are 18.5 mm and 9.1 mm, respectively. The average contact localization error for the proximal contact force of the DiC method and the data-driven approach are 6.9 mm and 4.1 mm, respectively. The average localization errors of the 2D and 3D experiments are summarized in Fig.6. The experimental results of the experiments can be seen in the accompanying video. One can notice that the estimated contact points of the newly proposed data-driven method converge more quickly to the position where the external forces are applied compared to the DiC approach.

The experimental results indicate that the here proposed framework outperforms the DiC approach in estimating the contact locations along the catheter length. An advantage of the proposed framework over other methods in the art is the ability to estimate the curvatures caused by external forces without knowing the input-output behavior. It is thus not needed to know the current input signal of the actuators. Thank to this feature, after knowing the contact locations the magnitude and the direction of the forces can be computed using the method described in [7]. In our prior work [19], the contact state estimation method was implemented based on an AutoEncoder. This AutoEncoder-based collision detection requires training a neural network to adapt to a new FR. The here proposed contact state estimation approach directly compares the output of the free-space curvature models to a threshold value which allows it to detect contact events. Thus, the new approach can be easily adapted to another FR without spending extra effort on training AutoEncoder. Since the data-driven free-space curvature models are used to learn the relations between curvatures at different points along the catheter length, the proposed framework can also be used in case a multi-core fiber is inserted into an off-centered channel of the FR. However, in this case, the curvatures measured by the fiber do not indicate the catheter's curvatures. Due to this reason, an extra calibration step should be done to find the mapping function between the measured curvatures and the catheter's curvatures. A detailed calibration step can be found in [21]. The current implementation of the proposed framework is done with MATLAB and runs at 10 Hz. The processing time of the contact localization framework could be further improved by using parallel computing.

IV. CONCLUSIONS

This paper presents a new data-driven multi-contact localization framework that consists of a contact event detection method and a contact localization method. The proposed approach requires only the curvatures along the catheter length to be measured by a multi-core FBG fiber inserted either in a centered or off-centered channel. The experimental results show that the data-driven contact estimation framework can detect the contacts in approximately 0.44*s*. Considering both 2D and 3D experiments, the here proposed contact localization method yields a consistent average contact localization error of 6.1 mm (1.6% of a sensed length of 370 mm), while the average contact localization of the DiC approach is 18.0 mm (4.9% of the sensed length). The contact localization error of the DiC approach varies depending on the contact location and the magnitude of the contact force. Moreover, the data-driven

contact localization approach also performs better in estimating the contact location of low-magnitude forces. In the future, the contact locations estimated by this data-driven framework will be used to estimate the direction and magnitude of the external force.

REFERENCES

[1] X. Lv, Z. Wu, C. Jiang, Y. Li, X. Yang, Y. Zhang, and N. Zhang, "Complication risk of endovascular embolization for cerebral arteriovenous malformation," *European journal of radiology*, vol. 80, no. 3, pp. 776–779, 2011.

[2] P. Valdastri, K. Harada, A. Menciassi, L. Beccai, C. Stefanini, M. Fujie, and P. Dario, "Integration of a miniaturised triaxial force sensor in a minimally invasive surgical tool," *IEEE transactions on biomedical engineering*, vol. 53, no. 11, pp. 2397–2400, 2006.

[3] P. Polygerinos, L. D. Seneviratne, R. Razavi, T. Schaeffter, and K. Althoefer, "Triaxial catheter-tip force sensor for mri-guided cardiac procedures," *IEEE/ASME Transactions on mechatronics*, vol. 18, no. 1, pp. 386–396, 2012.

[4] K. Yokoyama, H. Nakagawa, D. C. Shah, H. Lambert, G. Leo, N. Aeby, A. Ikeda, J. V. Pitha, T. Sharma, R. Lazzara *et al.*, "Novel contact force sensor incorporated in irrigated radiofrequency ablation catheter predicts lesion size and incidence of steam pop and thrombus," *Circulation: Arrhythmia and Electrophysiology*, vol. 1, no. 5, pp. 354–362, 2008.

[5] Y. Noh, H. Liu, S. Sareh, D. S. Chathuranga, H. Würdemann, K. Rhode, and K. Althoefer, "Image-based optical miniaturized three-axis force sensor for cardiac catheterization," *IEEE Sensors Journal*, vol. 16, no. 22, pp. 7924–7932, 2016.

[6] J. Back, L. Lindenroth, K. Rhode, and H. Liu, "Three dimensional force estimation for steerable catheters through bi-point tracking," *Sensors and Actuators A: Physical*, vol. 279, pp. 404–415, 2018.

[7] F. Khan, R. J. Roesthuis, and S. Misra, "Force sensing in continuum manipulators using fiber bragg grating sensors," in *2017 IEEE/RSJ International Conference on Intelligent Robots and Systems (IROS)*. IEEE, 2017, pp. 2531–2536.

[8] F. Feng, W. Hong, and L. Xie, "A learning-based tip contact force estimation method for tendon-driven continuum manipulator," *Scientific Reports*, vol. 11, no. 1, p. 17482, 2021.

[9] T. Li, C. Shi, and H. Ren, "Three-dimensional catheter distal force sensing for cardiac ablation based on fiber bragg grating," *IEEE/ASME transactions on mechatronics*, vol. 23, no. 5, pp. 2316–2327, 2018.

[10] A. Gao, N. Liu, H. Zhang, Z. Wu, and G.-Z. Yang, "Spiral fbg sensors-based contact detection for confocal laser endomicroscopy," *Biosensors and Bioelectronics*, vol. 170, p. 112653, 2020.

[11] O. Al-Ahmad, M. Ourak, J. Vlekken, E. Lindner, and E. Vander Poorten, "Three-dimensional catheter tip force sensing using multi-core fiber bragg gratings," *Frontiers in Robotics and AI*, vol. 10, p. 31.

[12] A. Bajo and N. Simaan, "Finding lost wrenches: Using continuum robots for contact detection and estimation of contact location," in *2010 IEEE international conference on robotics and automation*. IEEE, 2010, pp. 3666–3673.

[13] V. Aloi, K. T. Dang, E. J. Barth, and C. Rucker, "Estimating forces along continuum robots," *IEEE Robotics and Automation Letters*, vol. 7, no. 4, pp. 8877–8884, 2022.

[14] M. A. Diezinger, B. Tamadazte, and G. J. Laurent, "3d curvature-based tip load estimation for continuum robots," *IEEE Robotics and Automation Letters*, vol. 7, no. 4, pp. 10 526–10 533, 2022.

[15] Q. Qiao, D. Willems, G. Borghesan, M. Ourak, J. De Schutter, and E. Vander Poorten, "Estimating and localizing external forces applied on flexible instruments by shape sensing," in *2019 19th International Conference on Advanced Robotics (ICAR)*. IEEE, 2019, pp. 227–233.

[16] Q. Qiao, G. Borghesan, J. De Schutter, and E. Vander Poorten, "Force from shape—estimating the location and magnitude of the external force on flexible instruments," *IEEE Transactions on Robotics*, vol. 37, no. 5, pp. 1826–1833, 2021.

[17] O. Al-Ahmad, M. Ourak, J. Vlekken, and E. Vander Poorten, "Fbg-based estimation of external forces along flexible instrument bodies," *Frontiers in Robotics and AI*, vol. 8, p. 718033, 2021.

[18] C. M. Heunis, V. Belfiore, M. Vendittelli, and S. Misra, "Reconstructing endovascular catheter interaction forces in 3d using multicore optical shape sensors," in *2019 IEEE/RSJ International Conference on Intelligent Robots and Systems (IROS)*. IEEE, 2019, pp. 5419–5425.

[19] X. T. Ha, D. Wu, C.-F. Lai, M. Ourak, G. Borghesan, A. Menciassi, and E. Vander Poorten, "Contact localization of continuum and flexible robot using data-driven approach," *IEEE Robotics and Automation Letters*, vol. 7, no. 3, pp. 6910–6917, 2022.

[20] J. P. Moore and M. D. Rogge, "Shape sensing using multi-core fiber optic cable and parametric curve solutions," *Optics express*, vol. 20, no. 3, pp. 2967–2973, 2012.

[21] X. T. Ha, D. Wu, M. Ourak, G. Borghesan, J. Dankelman, A. Menciassi, and E. Vander Poorten, "Shape sensing of flexible robots based on deep learning," *IEEE Transactions on Robotics*, 2022.

[22] S. Sefati *et al.*, "Learning to detect collisions for continuum manipulators without a prior model," in *Intl. Conf. on Med. Imag. Comput. and Computer-Assisted Intervention*. Springer, 2019, pp. 182–190.

[23] G. Guo, H. Wang, D. Bell, Y. Bi, and K. Greer, "Knn model-based approach in classification," in *On The Move to Meaningful Internet Systems 2003: CoopIS, DOA, and ODBASE: OTM Confederated International Conferences, CoopIS, DOA, and ODBASE 2003, Catania, Sicily, Italy, November 3-7, 2003. Proceedings*. Springer, 2003, pp. 986–996.

[24] R. J. Webster III and B. A. Jones, "Design and kinematic modeling of constant curvature continuum robots: A review," *The International Journal of Robotics Research*, vol. 29, no. 13, pp. 1661–1683, 2010.

[25] R. Killick, P. Fearnhead, and I. A. Eckley, "Optimal detection of changepoints with a linear computational cost," *Journal of the American Statistical Association*, vol. 107, no. 500, pp. 1590–1598, 2012.

[26] C. B. Barber, D. P. Dobkin, and H. Huhdanpaa, "The quickhull algorithm for convex hulls," *ACM Transactions on Mathematical Software (TOMS)*, vol. 22, no. 4, pp. 469–483, 1996.

[27] M. Quigley, K. Conley, B. Gerkey *et al.*, "Ros: an open-source robot operating system," in *ICRA workshop on open source software*, vol. 3, no. 3.2. Kobe, Japan, 2009, p. 5.

[28] B. Zheng, Z. Janmohamed, and C. MacKenzie, "Reaction times and the decision-making process in endoscopic surgery," *Surgical Endoscopy and Other Interventional Techniques*, vol. 17, pp. 1475–1480, 2003.